SANDIA REPORT

SAND2005-7335
Unlimited Release
Printed November 2005

Geomechanics of penetration: Laboratory analog experiments using a modified split Hopkinson pressure bar/impact testing procedure

Glen L. Gettemy, David J. Holcomb, and David R. Bronowski

Prepared by
Sandia National Laboratories
Albuquerque, New Mexico 87185 and Livermore, California 94550

Sandia is a multiprogram laboratory operated by Sandia Corporation,
a Lockheed Martin Company, for the United States Department of Energy's
National Nuclear Security Administration under Contract DE-AC04-94-AL85000.

Approved for public release; further dissemination unlimited.

Sandia National Laboratories

Issued by Sandia National Laboratories, operated for the United States Department of Energy by Sandia Corporation.

NOTICE: This report was prepared as an account of work sponsored by an agency of the United States Government. Neither the United States Government, nor any agency thereof, nor any of their employees, nor any of their contractors, subcontractors, or their employees, make any warranty, express or implied, or assume any legal liability or responsibility for the accuracy, completeness, or usefulness of any information, apparatus, product, or process disclosed, or represent that its use would not infringe privately owned rights. Reference herein to any specific commercial product, process, or service by trade name, trademark, manufacturer, or otherwise, does not necessarily constitute or imply its endorsement, recommendation, or favoring by the United States Government, any agency thereof, or any of their contractors or subcontractors. The views and opinions expressed herein do not necessarily state or reflect those of the United States Government, any agency thereof, or any of their contractors.

Printed in the United States of America. This report has been reproduced directly from the best available copy.

Available to DOE and DOE contractors from
U.S. Department of Energy
Office of Scientific and Technical Information
P.O. Box 62
Oak Ridge, TN 37831

Telephone: (865) 576-8401
Facsimile: (865) 576-5728
E-Mail: reports@adonis.osti.gov
Online ordering: http://www.doe.gov/bridge

Available to the public from
U.S. Department of Commerce
National Technical Information Service
5285 Port Royal Rd
Springfield, VA 22161

Telephone: (800) 553-6847
Facsimile: (703) 605-6900
E-Mail: orders@ntis.fedworld.gov
Online ordering: http://www.ntis.gov/ordering.htm

SAND2005-7335
Unlimited Release
Printed November 2005

Geomechanics of penetration: Laboratory analog experiments using a modified split Hopkinson pressure bar/impact testing procedure

Glen L. Gettemy David J. Holcomb
David R. Bronowski

Geomechanics Department (6117)
Sandia National Laboratories
P.O. Box 5800
Albuquerque, NM 87185-9999
principal author contact: glgette@sandia.gov

Abstract

This research continues previous efforts to re-focus the question of penetrability away from the behavior of the penetrator itself and toward understanding the dynamic, possibly strain-rate dependent, behavior of the affected materials. A modified split Hopkinson pressure bar technique is prototyped to determine the value of reproducing the stress states, and mechanical responses, of geomaterials observed in actual penetrator tests *within* a laboratory setting. Conceptually, this technique simulates the passage of the penetrator surface past any fixed point in the penetrator trajectory by allowing for a controlled stress-time function to be transmitted into a sample, thereby mimicing the 1D radial projection inherent to analyses of the cavity expansion problem. Test results from a suite of weak (unconfined compressive strength, or UCS, of 22 MPa) concrete samples, with incident strain rates of 100-250 s^{-1}, show that the complex mechanical response includes both plastic and anelastic wave propagation, and is critically dependent on incident particle velocity and saturation state. For instance, examination of the transmitted stress-time data, and post-test volumetric measurements of pulverized material, provide independent estimates of the plasticized zone length (1-2 cm) formed for incident particle velocity of $\sim$16.7 m/s. The results also shed light on the elastic or energy propagation property changes that occur in the concrete. For example, the pre- and post-test zero-stress elastic wave propagation velocities show that the Young's modulus drops from $\sim$19 GPa to $<$8 GPa for material within the first centimeter from the plastic transition front, while the Young's modulus of the dynamically confined, axially-stressed (in 6-18 MPa range) plasticized material drops to 0.5-0.6 GPa. The data also suggest that the critical particle velocity for formation of a plastic zone in the weak concrete is 13-15 m/s, with increased saturation tending to increase the critical particle velocity limit. Overall, the data produced from these experiments suggests that further pursuit of this approach is warranted for penetration research but also as a potential new method for dynamic testing of materials.

Acknowledgment

Thanks to Robert Hardy (6117) for data acquisition support and many fruitful discussions.

Contents

1 Overview **10**

2 Description of experimental apparatus **12**

2.1 Stress-strain calibration 13

2.1.1 Strain gage measurements on incident bar and momentum trap 13

2.1.2 PZT pinducer recordings 14

3 Sample preparation and material property measurements **18**

3.1 Sample preparation 19

3.2 Material property measurements 20

4 Experimental results **21**

4.1 Stress-time results 21

4.2 Post-test observations 23

4.2.1 Microstructural integrity assessment using V_p measurements 23

5 Discussion **32**

5.1 Energy propagation and plastic work 32

5.2 Comparison to previous penetrator-simulation field tests (SAND2004-5211) 34

6 Conclusions and recommendations **36**

List of Figures

1.1 Post-penetration mechanical states of initially homogeneous material 11

2.1 Hopkinson impact test apparatus showing schematic and laboratory picture. 13

2.2 Breech pressure-stress calibration for incident bar. 14

2.3 Time histories for *elastic* compressive pulse from hammer tap test. 17

4.1 Estimated momentum bar stress and sample pinducer history for <0819> sample set. All samples were oven-dried, with P_{br}=(10, 25, 40) psi, respectively. 25

4.2 Estimated momentum bar stress and sample pinducer history for <0811> sample set, the high porosity (>30%) end-member. All samples were oven-dried, with P_{br}= 40 psi. The waveform at the bottom of the pinducer data plot is the trigger signal. 26

4.3 Estimated stress (in momentum bar) and sample pinducer history for <0906> sample set, to address effects of both saturation and P_{br} variability. 27

4.4 Post-test pictures illustrating the zone of pulverized concrete at sample front. 28

4.5 Post-test radial V_p measurements for sample set <0819>. 29

4.6 Post-test radial V_p measurements for sample set <0811>. 30

4.7 Post-test radial V_p measurements for sample set <0906>. 31

5.1 Apparent energy dispersion observed in momentum trap strain. 33

5.2 Effective *penetration* depth as a function of peak penetrator particle velocity. 35

List of Tables

4.1 Experimental program and results, including estimates of incident bar peak stress and particle velocity, crushed pore volume, and fractional V_p changes. 22

Chapter 1

Overview

The fundamental goal of this research is to reproduce experimentally the $\sim$1D cavity expansion/energy propagation mechanics inherent to penetration into an half-space. This process has been successfully modeled in terms of penetration depth estimation, for specific conditions, in theoretical (Forrestal, 1986; Forrestal and Tzou, 1997) and numerical work(Fossum, 2004; Warren et al., 2004). Validation of predicted material responses, and hence of the constitutive representation of the material, has not been extensively reported. Indeed, few penetrator experiments (e.g., Gran and Frew, 1997) have had data acquisition from which *in situ* material responses could be derived. In general, penetrator deceleration-penetration depth are the only variables measured (Forrestal et al., 2003; Frew et al., 2004). A method of testing that allows sufficient data to be recovered from an experiment with a precisely known stress-time input could thus prove quite valuable to further understanding of penetration mechanics.

Figure 1.1 illustrates the spatial distribution of energy propagation, and associated mechanical behavior, of a penetrated, initially homogeneous, material. Nearest the surface, the kinetic energy of the penetrator is transported away first as a plastic wave, then with transitions into possible cracked/anelastic, anelastic, and finally into elastic transport as energy is absorbed. The energy transport mechanism/mechanical behavior with depth, for material at the penetrator surface, reflects the critical velocity concept discussed in Forrestal (1986) and von Karmen and Duwez (1950). Note that except at the surface of the material, the penetrator actually pushes through pre-stressed, possibly plastically deformed, material so long as the penetrator velocity is slower than the energy transport wave speed of the pre-stressed material. This realization is one of the major shortcomings of the standard cavity expansion approach to penetration modeling. An experimental technique that allows for multiple loading cycles is thus needed to mimic the stress history that could be recorded along any particular path (e.g., trajectories 1 and 2, respectively, in Figure 1.1). The choice of experimental apparatus and experimental program reported in the remainder of this document follow from this brief introduction.

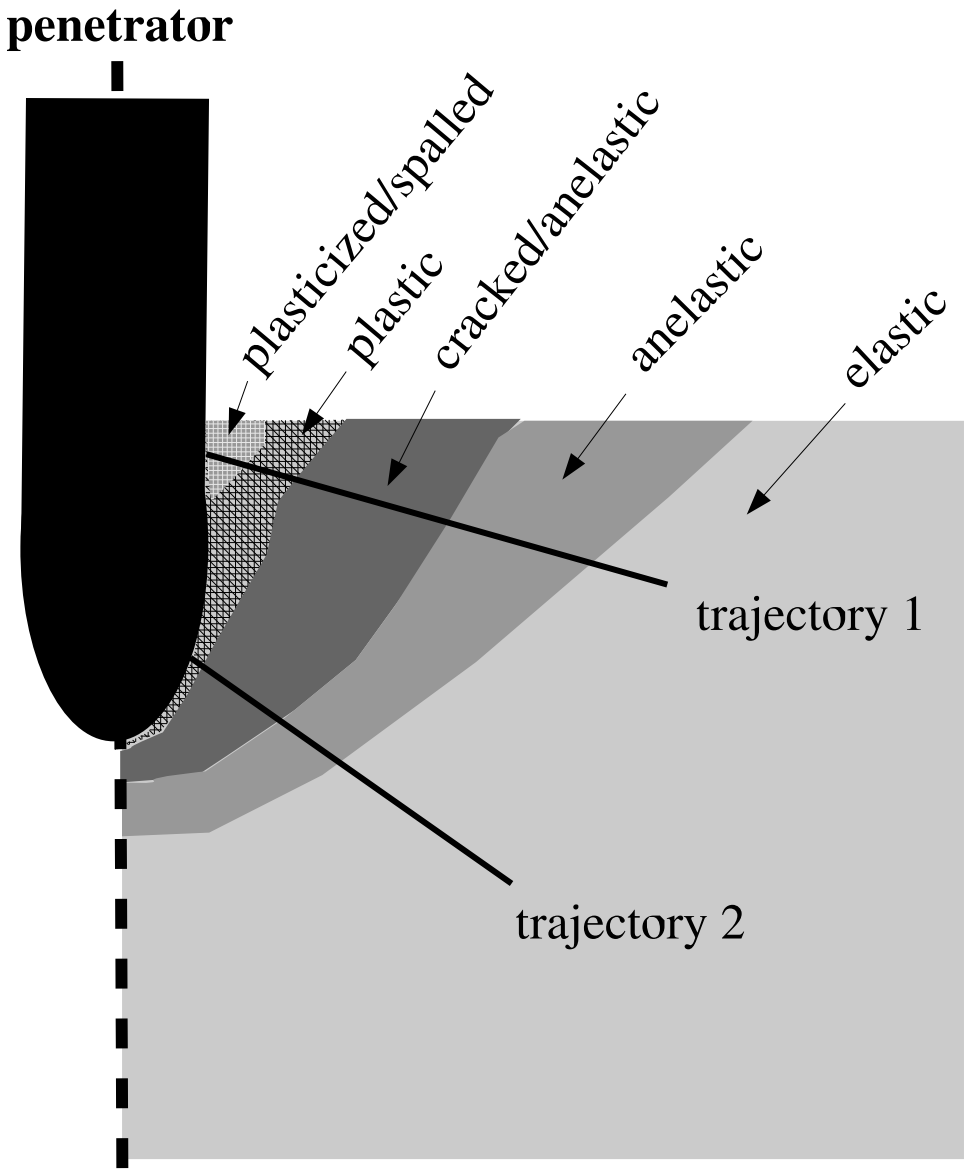

Figure 1.1. Post-penetration mechanical states of initially homogeneous material

Chapter 2

Description of experimental apparatus

The overarching requirement of the experimental approach is the need to generate a reproducible one dimensional stress wave–with strain rates >100 s^{-1} and particle velocities sufficient to recreate the plastic front observed in field penetrator experiments–and pass it *once* through a 15-20 cm long cylindrical bar. The simplest testing option appeared to be to modify the conventional split Hopkinson pressure bar (SHPB) scheme, which allows for stress wave control (Zheng et al., 1999; Frew et al., 2005), into an SHPB-impact testing apparatus (Figure 2.1). The modified system flyway consists of (i) a 2.54 cm diameter, 1.45 m long titanium incident bar equipped with a full-bridge strain gage array to measure axial strain, (ii) a 2.54 cm diameter, 15-20 cm long sleeved sample with a $\sim$10 MHz, 2 mm diameter shock-type piezoelectric transducer (pinducer) inserted at $\sim 30^o$ to the sample axis, and (iii) a 2.54 cm diameter, 50 cm long transmission bar, or *momentum trap*, with a half-bridge strain gage array to measure axial strain, whose elastic impedance matches the sample. If the sample and momentum trap impedances are matched, the stress wave that propagates through their interface will do so essentially unchanged, with negligible energy reflected at their contact. Operation of the SHPB/impact apparatus is identical to standard SHPB protocols, with the exception that data from within the sample is collected. All strain gage and pinducer waveforms are sampled at 1.0 MHz, which is $>$8X the maximum useable frequencies in the incident bar stress wave. Both the strain gage data acquisition and oscilloscope are triggered by a PZT crystal mounted $\sim$15 cm from the impact end of the incident bar. The pinducer and trigger signal are both recorded so that absolute time can be obtained for data analysis.

Note that this setup, when unstressed, introduces finite discontinuities at the incident bar-sample and sample-momentum trap interfaces. These mechanical boundaries complicate the experiment, especially the interpretation of the recorded strain-time data; this problem is described in the following section and discussed more fully in Chapter 5.

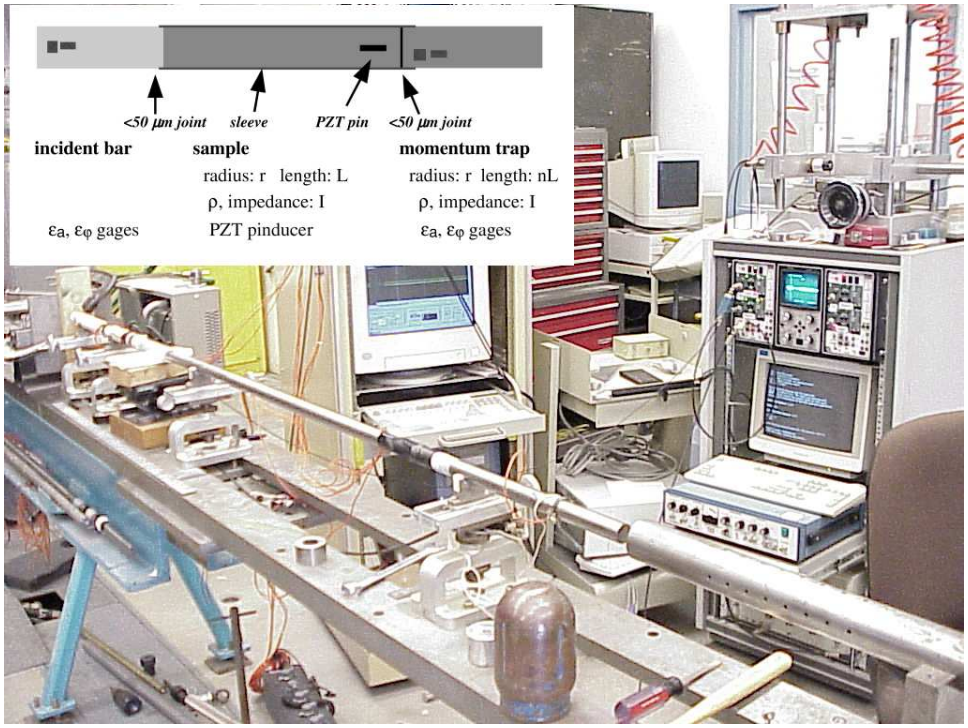

Figure 2.1. Hopkinson/impact test apparatus showing (inset) schematic and laboratory picture. Air gun muzzle is shown in foreground; sample and momentum trap are at far end of flyway.

2.1 Stress-strain calibration

2.1.1 Strain gage measurements on incident bar and momentum trap

Two separate calibrations associated with the incident bar were required. The first step was quasi-static load cell measurements with uniaxial stress <7 MPa to verify the axial strain readings. Two separate tests, on two different full-bridge gage arrays, resulted in volt-to-stress conversion constants of 5.756x10^9 Pa/V and 5.800x10^9 Pa/V, respectively; these are both within 1% of the theoretical calibration which includes the gage factor, gage input voltage, Young's modulus, and Poisson's ratio as variables in its calculation. The second component of incident bar calibration involved determining the stress-time histories that could be reproduced for a given series of breech pressures (P_{br}). Figure 2.2 provides a snapshot of the first pulse launched down the incident bar by a 8.9 cm long aluminum striker bar, with no pulse shaper added at the impact surface. Peak stress ranges from 166-375 MPa for the 10-40 psi breech pressures tested. Multiple shots show that these waveforms are extremely repeatable for a given pressure. The stress wave is associated with particle velocities of 7.4-16.7 m/s and strain rates of 100-250 s^{-1}. The main pulse width is $\sim$55 μs duration. The oscillatory component of the waveform, evident in the

initial pulse and increasing as the wave travels around the bar (Figure 2.2a,b), is due to the Pochhammer-Chree dispersion induced by the somewhat broad bandwidth signal created by the impact (Kolsky, 1963).

Independent stress-strain load cell calibration of the half-bridge gage array on the momentum trap proved unreliable due to (i) changing compliance at several joints, necessary only for the quasi-static loading arrangement when using the load cell, and (ii) possible flexure of the momentum trap. The theoretical calculation for that gaging geometry was therefor assumed for all axial stress conversions. Repeated hammer tap tests generating $\sim$10 MPa peak stress in the incident bar were consistently recorded throughout the experimental program, so while the actual conversion may be incorrect absolutely, gage coupling and overall performance appeared to remain unchanged. Elastic wave velocities were used to determine the low-stress effective Young's modulus for the concrete bar, which ranged over 18.5-20.0 GPa. A median value of 19.0 GPa was used for all conversions in this report.

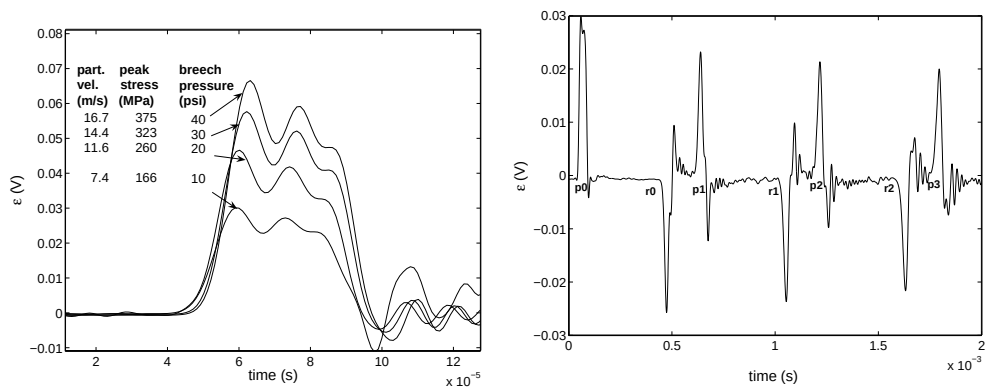

(a) Incident bar calibration **(b)** Multiple pulses at 10 psi

Figure 2.2. Breech pressure-stress calibration for incident bar. (a) Strain- time histories for initial compressional stress wave, with P_{br}=(10, 20, 30, 40) psi. (b) Strain-time history for 2.0 ms with P_{br}=10 psi.

2.1.2 PZT pinducer recordings

The use of (PZT) pinducers to directly record the strain waves within the sample is a new approach to such dynamic testing, though extensive use of these instruments has been previously reported (e.g., Olsson and Holcomb, 2000). Using crystal dimensions supplied by the manufacturer (Dynasen Incorporated, Goleta CA) and the range of PZT piezoelectric pressure constants in Krautkramer and Krautkramer (1983), the pinducers have a nominal response from 10.02-20.05 kPa V^{-1}; for report purposes, the minimum response will be used wherever pinducer output is transformed to an axial stress estimate (see below for further discussion). For future experiments, an independent calibration system needs to be

developed to allow for empirical determination of the pressure response *in situ*, without any factors other than crystal variability and pinducer-sample mechanical coupling involved in the resultant pressure constant.

Interpretation of the pinducer signals requires knowledge of the impulse response function for the pinducer. In the time domain, the impulse response function can be written, to first order, as the sum of two delta functions separated in time by the characteristic time-of-flight for a unit strain propagating through the PZT crystal. For stress waves with frequencies <0.001X the pinducer resonant frequency, and considering the brass backing of the pinducer, the pinducer should act as a differentiator of the input wave–in effect, as an accelerometer. This analysis is consistent with the opposite situation–a thick resonator driven by frequencies much greater than its resonance, which acts as a signal integrator (Silk, 1984). Figure 2.3a presents a time window of 200 μs around the initial pulse from hammer tap tests recorded by a single pinducer coupled with a viscous fluid (molasses). The peak stress in the bar, determined from the strain gage data, ranges from 8-11 MPa. The time derivative of the stress wave is shown (dashed lines) for comparison with the bottom data plot in Figure 2.3a which displays the pinducer waveforms. The large signal variability is due to both coupling differences and the true incident wave shape. Integration of the four largest signals over the time interval of positive pinducer output, or positive acceleration, allows estimation of the stress-time history up to the peak stress. The accuracy of the estimates ranges from $\pm$1-10%, using a pressure constant of 10.02 kPa V^{-1} as discussed above. Note that the pinducer response does not need to be corrected for the free surface effect. This short investigation suggests that the pinducers may yield valid stress estimates for the leading front of the stress wave, at least up to the initial peak stress. The behavior of the pinducer is suspect beyond the output minimum (Figure 2.3a), i.e., up to the time at which the particle acceleration reaches its minimum, probably due to instrument coupling.

Figures 2.3b,c show incident bar and momentum trap stress, and pinducer output voltage, for a synchronous 1 ms period from three separate hammer tap tests in which a 15 cm long aluminum bar, with pinducer located 12 cm from the Al bar front face, acts as a sample. Signal dispersion–e.g., comparing the signal duration in the incident bar (165 μs) versus the momentum trap (500 μs)–is observed in both the pinducer and momentum trap data. This suggests that the dispersion is occurring within the sample itself. The apparent reflection coefficient (-0.64), deduced from the ratio of the peak stress in the initial and reflected pulses on the incident bar, is much greater than would be expected for a titanium-aluminum welded interface (-0.22). This suggests that the interface, at both the incident bar-sample and sample-momentum trap, may effectively act as a stress-dependent compliant fracture in a similar, but not identical, fashion as described in Pyrak-Nolte et al., 1990). This interaction would increase the (absolute) value of the apparent reflection coefficient, and suggests that the interface acts as a time-dependent filter. For the Al bar, a simple 1D elastic wave propagation model, with the interfaces described as a finite-sized layer with effective Young's moduli of 2.5-6.0 GPa, replicates the general dispersion shown in Figure 2.3b. At low stresses, such as those generated by hammer tap tests, these interface discontinuities may not close completely, and thus allow for increased energy trapping within the sam-

ple. The signal captured in the pinducer recordings (Figure 2.3c) supports this analysis, and suggests that the pinducer mount and coupling–insertion into a pre-drilled hole at 30° to the sample axis, with the same couplant previously used–improves the deceleration response of the pinducers. Additional factors, such as other modes excited by the imperfect hammer-bar impact, may contaminate the data but still leave the rise time and peak stress estimates intact.

The preceeding discussion, with respect to both strain gage and pinducer data collection, suggests that two independent estimates of the initial peak stress and rise time can be made for the energy propagating through the sample. The momentum trap strain gage should record only information about energy transmitted through the sample and its interface with the momentum trap. Note that the momentum trap appears to be extremely efficient at absorbing energy that passes into it. Tests with a 2.54 cm diameter ultrasonic transducer, and later analysis of actual test results, show that no energy is reflected back across the strain gage array mounted on the momentum trap. With respect to the pinducer recordings, the waveforms can only be used to estimate the initial peak stress and track arrivals of pulses starting from the incident bar-sample interface (i.e., reverberations *p0, p1,* etc. in Figure 2.2).

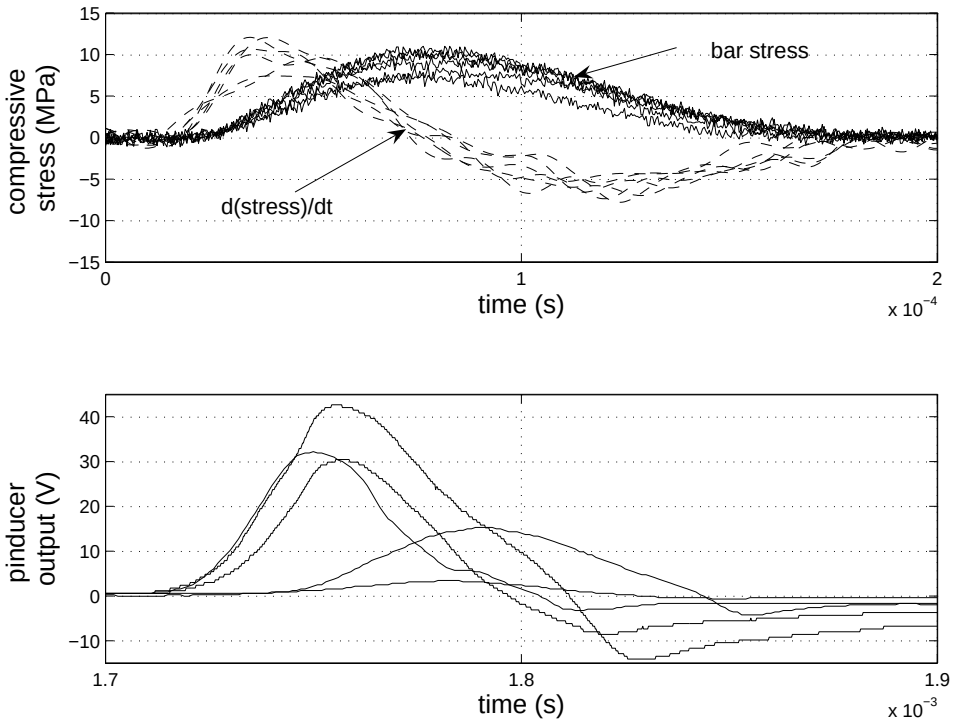

(a) Incident bar stress and its time derivative (top) compared to pinducer recording (bottom).

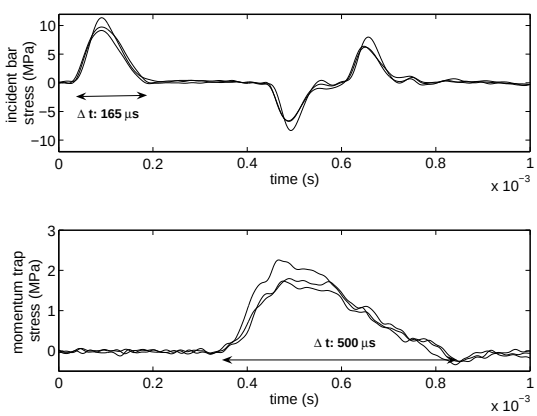

(b) Incident (top) and momentum trap stress (bottom) with 15 cm aluminum bar sample between incident and trap.

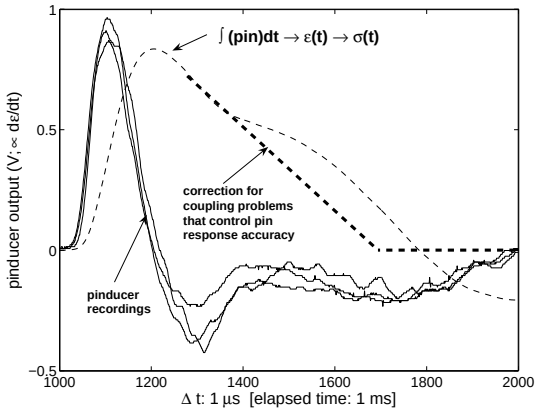

(c) Pinducer original and integrated output from mounting position at 12 cm from Al bar end, with pin oriented 30° from bar axis.

Figure 2.3. Time histories for *elastic* compressive pulse from hammer tap test.

Chapter 3

Sample preparation and material property measurements

The sample material is equivalent to that used in previous penetration work (Holcomb et al., 2005), a weak concrete (UCS=22MPa) containing negligible volume fraction of particles with nominal diameters >3 mm. This choice is crucial for several reasons. First, the particle size distribution should ensure approximate homogeneity of stress transfer over the 2.54 cm diameter incident bar surface area. For these experiments, the minimum bar:particle diameter ratio is ∼10. Second, this concrete mix is similar to materials used in the work of Frew et al. (2004) and Warren et al. (2004). Thus, the results produced herein may be applicable to understanding the deceleration data and modeling efforts reported in that earlier work.

Two key experimental considerations are the (i) sample geometry, and (ii) process by which the wet concrete mixture was placed into its final cylindrical shape. Sample length-to-diameter ratio of 6-8 was necessary to ensure that the gradient in material response could be controlled as has been seen in actual and simulated field trials (Frew et al., 2004; Holcomb et al., 2005). The 2.54 cm diameter of the incident bar thus set the sample length to 15-18 cm. For samples of this length, almost any flexural stress results in a catastrophic radial fracture, so a clear plexiglass tube, with wall thickness ∼3.5 mm and length of 30 cm, was selected to confine the samples throughout the production and testing stages of the program. These jackets had a front beveled end and 6-8 sets of diametrically-opposed ∼3 mm holes drilled in the first 18 cm. The inside walls of the front ende were machined to tightly fit a 15 mm-long smooth endcap which would be inserted during sample production. Each jacket was weighed to allow for physical property determination as described below.

Three unique sample sets (<0811>, <0819>, and <0906>), with each set consisting of five cylinders, were created and monitored for physical property homogeneity and temporal changes as described below. Chapter 4 describes the experimental program in detail.

3.1 Sample preparation

The concrete mix used in Holcomb et al. (2005) was used for all sample sets. The recipe (by weight [nominal volume of 1000 cm^3]: *ASTM (I/II) portland cement* - 0.306 kg; *sand* - 1.606 kg; *water* - 0.259 kg) was carefully dry-mixed, hydrated, and stirred in a large bucket. This material was then placed in a 10 cm diameter standard concrete testing container, fitted with a false bottom, and rodded/tapped for 3-4 minutes to promote settling. The container was then placed on a 60 Hz vibrator plate and run on the lowest amplitude setting for 1 minute. Vibration and tapping continued together for another minute, and then 2 or 3 of the jackets, beveled end down, were placed on the surface of the concrete. The vibrator amplitude was set at maximum amplitude and the jackets were pushed to the bottom, using 6-8 N of applied force to assist in the settling. Once the jacket end reached the bottom of the container, continued vibration filled the jackets (through the wall holes) to the depth of the concrete in the container. The jackets were then pushed out the false bottom of the container, the front $\sim$15 mm of the jacket was scraped out, and a endcap was inserted and taped in place. At this time, the concrete had a porosity of 27-35% (see <0811>). Further vibration of the jacketed samples reduces the porosity by mobilizing the trapped air up and out of the sample top. Sets <0819> (average porosity: 18%) and <0906> (average porosity: 20%) were processed for an additional 3 minutes.

Following mass and compressional wave time-of-flight measurements, which were completed within 60 minutes of the initial pour, the entire sample set, with endcaps removed, was placed in a laboratory oven, sample axis oriented horizontal, and dried at 40-45 ^oC for a minimum of 48 hours. This process essentially fixes the mechanical state of the concrete by removing water from the system. Mass and compressional wave time-of-flight measurements were made following removal from the oven. Samples were then trimmed to final length and $\sim$15 mm of jacket was machined off the sample back to allow the sample to slide into the front of the momentum trap jacket. A single pinducer was inserted into a pre-drilled hole through the sample jacket and $\sim$3 mm into the concrete itself. The pinducers for set <0811> used molasses as a couplant, which was smeared over the pin head prior to insertion. A quick-set epoxy was used to couple the pinducers for experiments on sets <0819> and <0906>. Sample front and back faces were capped, as necessary, with (i) cured plaster-of-paris, (ii) cured portland cement, or (iii) dry portland cement to create a smooth contact surface for the incident bar and momentum trap interfaces, respectively. The dry cement technique proved to be the most time-efficient as it did not require post-cure grinding. The added material was no more than $\sim$250 mm^3 for any single end face.

Three samples from <0906> were saturated with isopar, a kerosene-like hydrocarbon with viscosity $\simeq$1.7 cP, to study the effects of saturation state on stress propagation. The simple saturation procedure was to place the dried samples in a fluid bath, with isopar depth $\simeq$10 cm, and then allow the samples to stand for >24 hours.

3.2 Material property measurements

Sample mass and radial compressional wave velocity (V_p), as function of axial position, were monitored at the initial/pour, dry, and post-test states of the experimental program. Using the effective particle density (2555 kg m^{-3}) for the nearly identical concrete in Holcomb et al. (2005), dry density (ρ) and porosity (ϕ) can be readily determined by accounting for the loss of water between the initial and dry weight measurements. Compressional wave time-of-flight measurements and subsequent V_p derivations were obtained using the velocity bench and pulse-receive algorithm as in Holcomb et al. (2005).

Chapter 4

Experimental results

The experimental program involved tests on three distinct sample sets (Table 4.1). This program was designed to highlight the effects of porosity (20% versus 32%) and saturation state (dry *versus* fully-saturated) under dynamic stress states that varied in peak incident bar stress over 166-375 MPa, or peak incident bar particle velocities of 7.4-16.7 m/s. Beside porosity and V_p measurements, post-test estimates of crushed pore volume (V_{cr}) were also made to quantify the plastic deformation absorbed by the respective samples. V_{cr} measurements were made by multiplying the volume of concrete completely pulverized in a given sample by the measured porosity of the sample. The pulverized concrete volume was estimated by determining the volume of molding clay required to re-form the original sample volume in its jacket. Principal results of these tests are discussed in terms of the stress-time observations and post-test observations, respectively, in the following two sections.

4.1 Stress-time results

Estimated momentum bar stress and sample pinducer output recordings are shown in Figures 4.1- 4.3. These data contain the history of energy propagated through the sample associated with the initial and first reflected incident bar pulses (*p0* and *p1* in Figure 2.2, respectively). A comparison of the *p0* versus *p1* data illustrates how the constitutive behavior of the concrete changes following a penetration event. This change is a key concern for modeling efforts focused beyond the cavity expansion paradigm. Note that in all three cases studied, the character of the transmitted stress waveform changes significantly between the first and second pulse. The validity of the reported pinducer peak stress estimate is judged to be low due to inconsistencies within and between the sample sets. A review of each dataset is briefly provided below.

Figure 4.1 depicts results from set <0819> (ϕ: 19%) for P_{br} ranging from 10-40 psi or, equivalently, peak incident bar stress of 166-375 MPa. The transmitted stress increases with increasing incident stress, in both the momentum bar recording and the pinducer-

Table 4.1. Experimental program and results, including estimates of incident bar peak stress and particle velocity, crushed pore volume, and fractional V_p changes. Notes: [1] - $V_{p,nom}$, was estimated as the mean V_p measurements obtained within the 9-15 cm range (relative to the impact end of a sample; [2] - associated with the lower P_{br} test; [3] - used dry pre-test V_p data to establish $V_{p,nom}$; [4] - axial distance from impact end of sample.

set	#	porosity (%)	sat/dry	P_{br} (psi)	max(σ_{inc}) (MPa)	max(v_{inc}) (m/s)	$V_p/V^{(1)}_{p,nom}$ (3.5,5.5,7.5)[4] cm	V_{cr} (cm^3)
0811	1	27	dry	40	375	16.7	0.61,0.84,1.01	1.0
	2	35	dry	40	375	16.7	0.64,0.94,0.96	2.1
	4	33	dry	40	375	16.7	0.63,0.92,0.94	2.6
	5	36	dry	40	375	16.7	0.68,1.00,0.94	3.1
0819	1	17	dry	40	375	16.7	0.62,0.89,1.01	1.9
	2	19	dry	40	375	16.7	<0.5,0.88,1.02	1.5
	3	19	dry	10	166	7.4	0.84,0.95,0.94	0.1
	4	17	dry	40	375	16.7	<0.5,0.88,1.02	1.7
	5	19	dry	25	290	13.0	0.67,0.88,0.99	0.2
0906	1	20	sat	25	290	13.0	0.90,1.10,1.66	0
	2	20	sat	10/25	166[2]	7.4[2]	0.55,0.88,1.03[3]	0
	3	19	sat	40	375	16.7	0.87,0.89,1.03	1.8
	4	20	dry	10	166	7.4	0.97,0.92,1.07	0.2

based integrated peak estimate. Figure 4.2 presents recordings from the dry, high-porosity (∼32%) samples of set <0811>, all of which were tested at an incident bar peak stress of 375 MPa. The momentum bar stress-time recordings for *p0* appear to segregate into two clusters, but the differences largely disappear (after accounting for the initial offset at 0.9 ms) for the *p1* pulse. The pinducer data accurately record only the rise in the received stress wave for *p0* due to coupling with molasses. Figure 4.3a reports momentum bar stress-time results from the saturated samples tested at 166-375 MPa, with a dry sample also tested at the lowest incident stress level shown for comparison. The pinducer data (Figure 4.3b) show only the saturated tests results, including the P_{br}=25 psi (300 MPa) recording of the previously-tested, or *reshot* test, sample. Both waveforms show greater complexity than the dry concrete results. Indeed, comparison between these data and the dry analogs of <0819> is complicated not only by any saturation effect on the constitutive behavior of the concrete itself, but also by the significant change such behavior has on stress transfer at the incident bar-sample and sample-momentum trap interfaces.

Discussion beyond these simple observations is difficult. The variability in resultant stress-time and peak stress estimates between the pinducer and momentum trap data, from sample to sample both within a set and between sets, is sufficiently large and apparently inconsistent that issues of physical consistency of samples and interface conditions can not be ruled out as determining causes in the result fluctuations. Suggestions are provided at the end

of the report for improving this situation for future experiments. Interestingly, the peak stress measurements from the momentum bar data are consistent with UCS test results in Holcomb et al. (2005), which indicate a peak strength of 7-11 MPa for samples of this age. The sample preparation for the UCS-tested samples in Holcomb et al. (2005) is very different from the protocol followed in this study, however, as the mechanical state of these samples was essentially fixed by removing free moisture with ∼48 hours after the initial pour.

4.2 Post-test observations

Pictures of post-test samples are shown in Figure 4.4. The destruction of the sample front clearly shows the extent of the final penetration and plasticized volume. For the dry samples, the sample front was always pulverized to some extent, while saturation prevented such destruction for incident bar peak stress up to ∼300 MPa, or particle velocities of 13.0 m/s (Figure 4.4c). The comminution was complete to a dry powder, with no fragments larger than single sand grains visible in the material that could be recovered. Sample jackets failed, most likely after *p0* and *p1* pulses, for all tests with P_{br}=40 psi.

4.2.1 Microstructural integrity assessment using V_p measurements

V_p measurements are used to provide a metric on the microstructural state of each sample at the pour, oven-dried, and post-test states. Figures 4.5- 4.7 contain the discrete measurements made on sets <0819>, <0811>, and <0906>, respectively. Measurements of V_p made on the just-poured samples show an essentially homogeneous state for each particular sample, with small sample-sample variability (±3%) relative to the mean measurement for a respective set. Dry V_p measurements (small symbols, with lines) show more variability both spatially, within a sample (±5%), and between samples of a particular set. The apparent V_p reduction in pre-test dry measurements (<2900 m/s) at the sample front generally results from the proximity of the sample boundary relative to the placement of the transducers used to conduct the wave propagation experiment. For <0819>, the dry measurements shown in Figure 4.5 appear to be strongly influenced by a partial saturation effect, i.e., the gradient from the sample front to 7 cm, which may have occurred because of a short oven-time exposure. The *true* dry velocities–which were spot-checked following additional oven drying and 48 hours of open-air cooling–are actually consistent with the post-test measurement for 9-15 cm, similar to the dry V_p data for <0811> (Figure 4.6). Over all three datasets, the *true* pre-test dry V_p fall into a 2900-3500 m/s range.

Post-test V_p measurements for the dry samples show a very consistent velocity reduction that is clearly controlled by incident bar stress transfer. Figure 4.5 illustrates this with schematic curves that track the V_p profile typified by the samples tested at 166, 300, and 375 MPa incident bar peak stress, respectively. Table 4.1 shows these data normalized

by the mean pre-test dry V_p. The extent of the microstructural deformation ranges from 5-8 cm with relative V_p reduction of 0.8-0.5 times, at the sample front, over the 166-375 MPa test range. The results for set <0811> (Figure 4.6) are consistent with Figure 4.5, suggesting the higher porosity (32% versus 19%) does not significantly change the extent of the damaged region that extends 8 cm into the sample for σ_{inc}^{pk}=375 MPa.

The saturated tests (Figure 4.7) produced a much more complicated picture of microstructural change, compounded by fluid saturation effects at the high frequencies (>500 kHz) used to conduct the cross-axis V_p measurements. In fact, the large difference between pre-test dry and post-test (at least partially) saturated measurements (samples 1 and 2) support the assertion of fluid effects in the initial results for supposedly dry pre-test samples of <0819>. Fluid-saturated sample 3–tested at incident bar peak stress of 375 MPa, or $v_{part} \simeq$16.7 m/s–shows no signs of microstructural damage beyond the 1.8 cm-long pulverized sample front. A significant change in V_p is seen for sample 2 following a P_{br} test at 10 psi, though this difference is likely associated with the local saturation state of the sample within the 4-9 cm domain. A second test of sample 2, however, at P_{br}=25 psi results in a completely different outcome, both with respect to its previous test and compared to the test results of sample 1. 300 MPa peak incident stress, or peak $v_{part} \simeq$13.0 m/s, appears to induce a large microstructural deformation gradient in the concrete. The net effect of saturation and microstructural change is thus likely dependent on the local porosity-permeability systematics of a specific sample. Note that neither sample experienced any pulverizing of the sample front. Further testing and modeling will be required to sort out the apparent conundrum between results of samples 1 and 2 relative to those of sample 3.

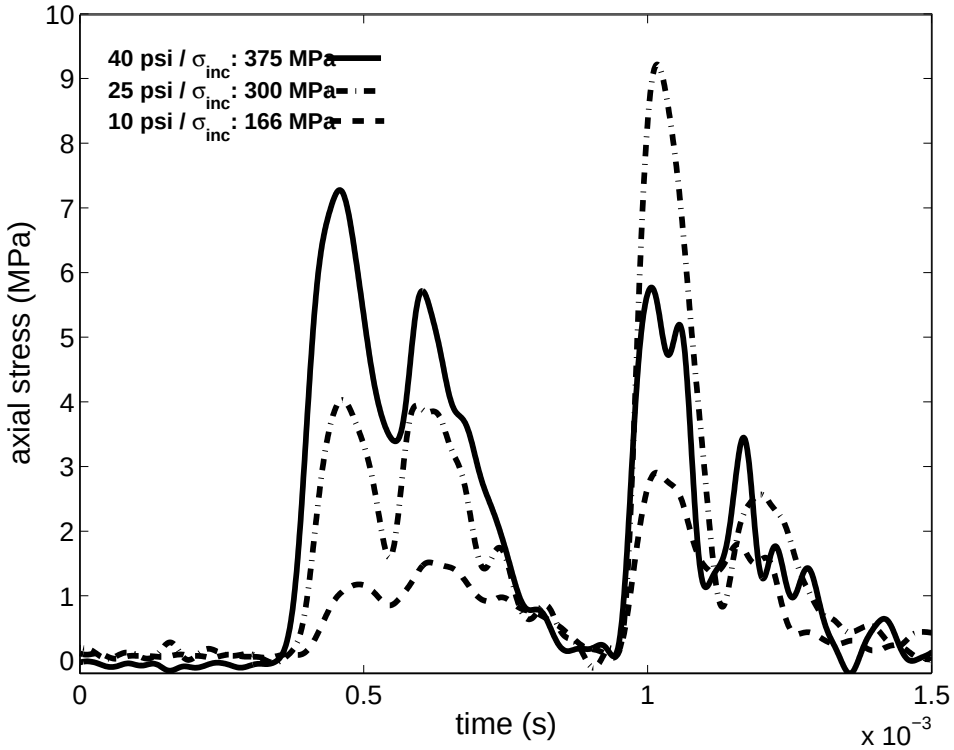

(a) Momentum bar (ε-gage)

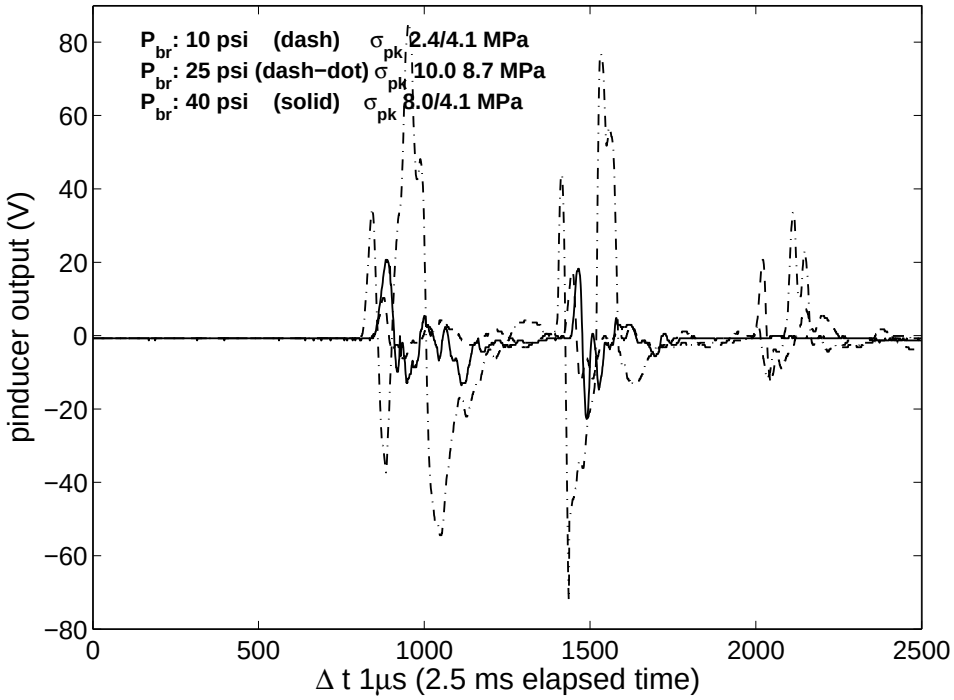

(b) Sample pinducer

Figure 4.1. Estimated momentum bar stress and sample pinducer history for <0819> sample set. All samples were oven-dried, with P_{br}=(10, 25, 40) psi, respectively.

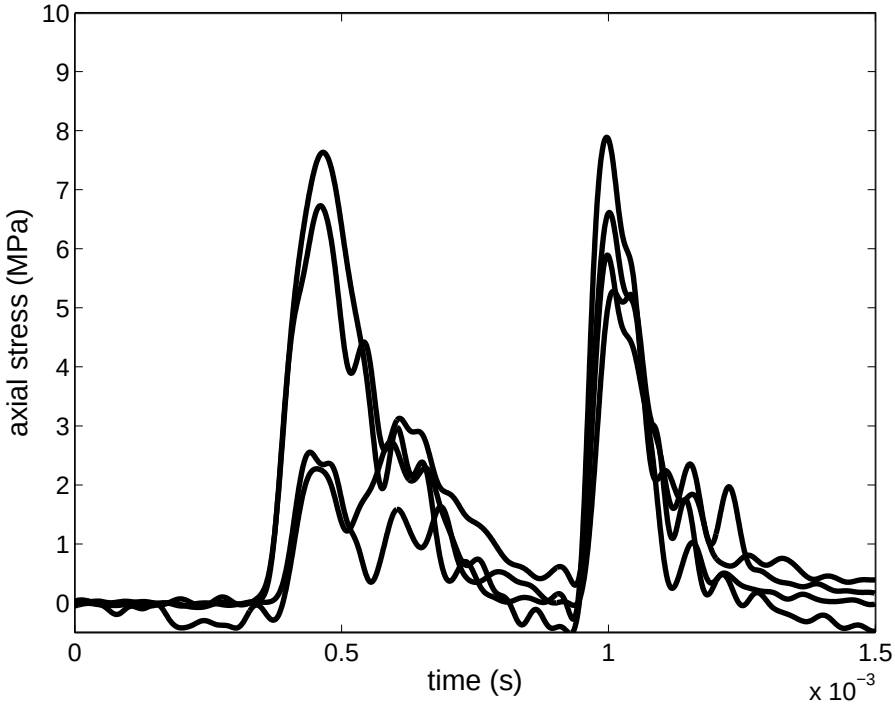

(a) Momentum bar (ε-gage)

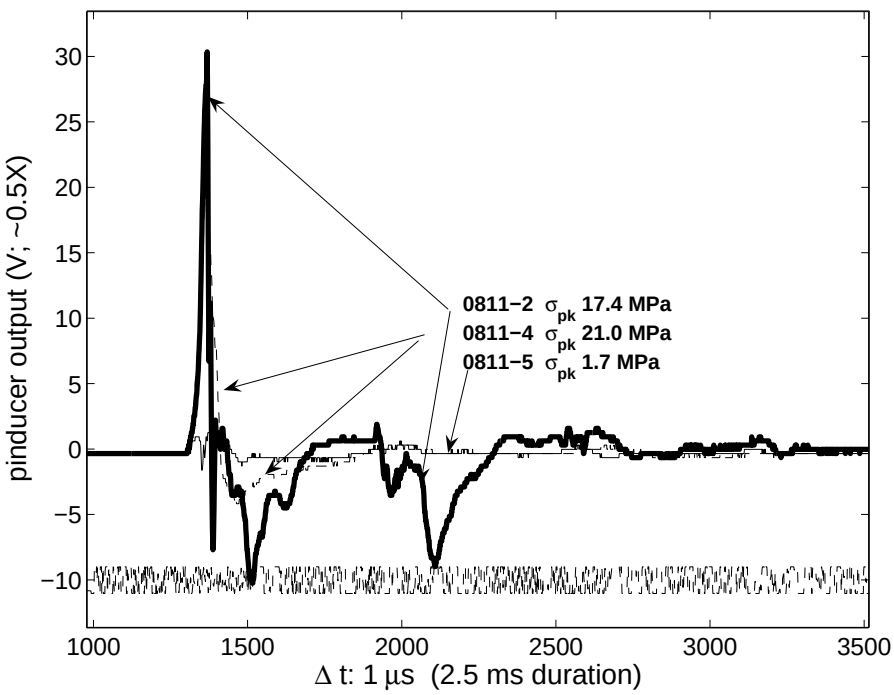

(b) Sample pinducer

Figure 4.2. Estimated momentum bar stress and sample pinducer history for <0811> sample set, the high porosity (>30%) end-member. All samples were oven-dried, with P_{br}= 40 psi. The waveform at the bottom of the pinducer data plot is the trigger signal.

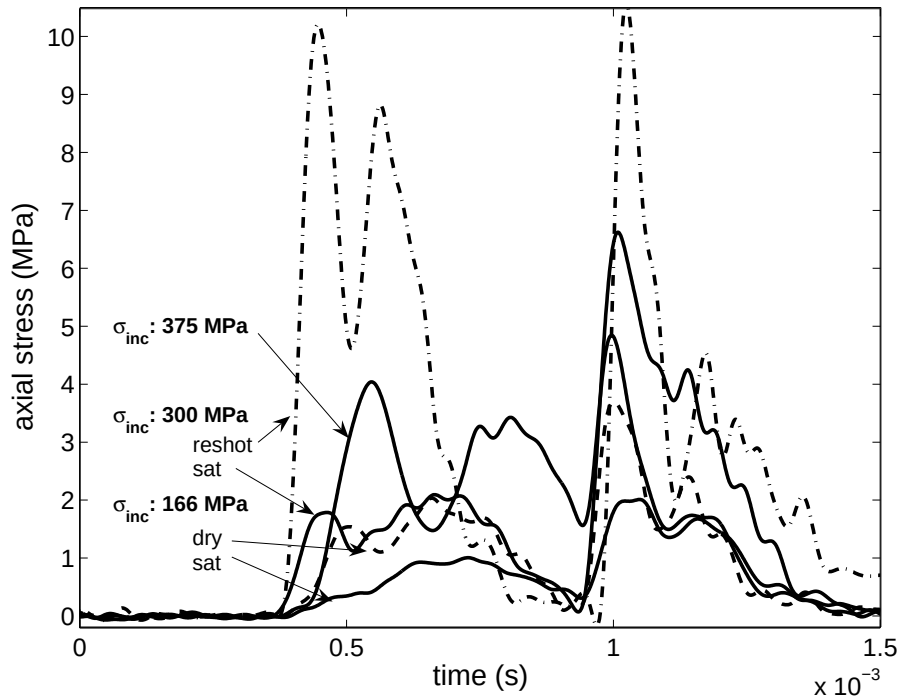

(a) Momentum bar (ε-gage)

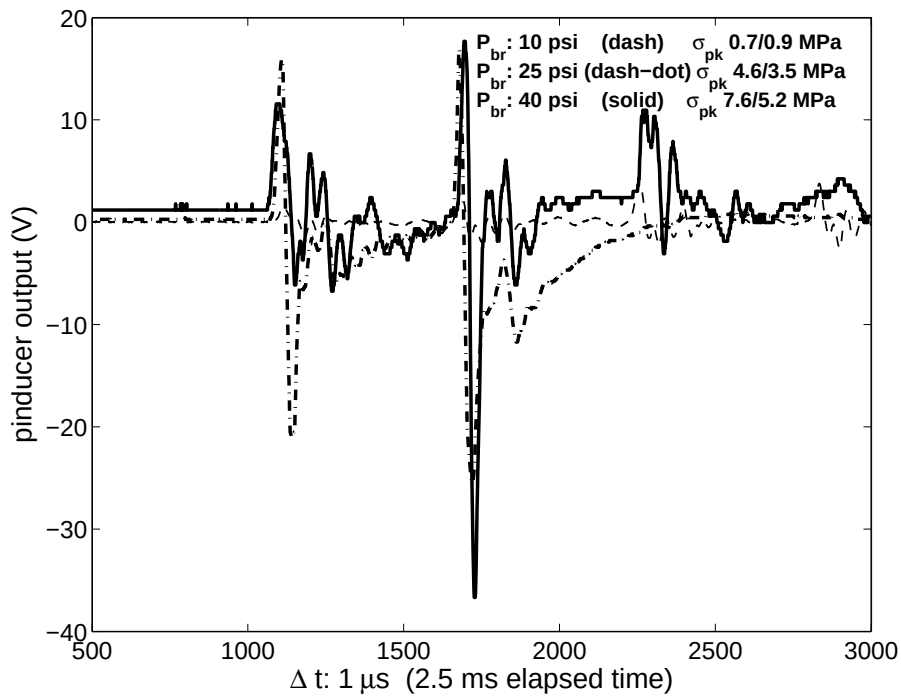

(b) Sample pinducer

Figure 4.3. Estimated stress (in momentum bar) and sample pinducer history for <0906> sample set, to address effects of both saturation and P_{br} variability.

(a) (Dry) test at P_{br}=40 psi

(b) Single pour (dry) tests at P_{br}=40 psi, sample set <0811>.

(c) (Saturated) test at P_{br}=25 psi

Figure 4.4. Post-test pictures illustrating the zone of pulverized concrete at sample front. Results are dependent on both incident stress state and saturation.

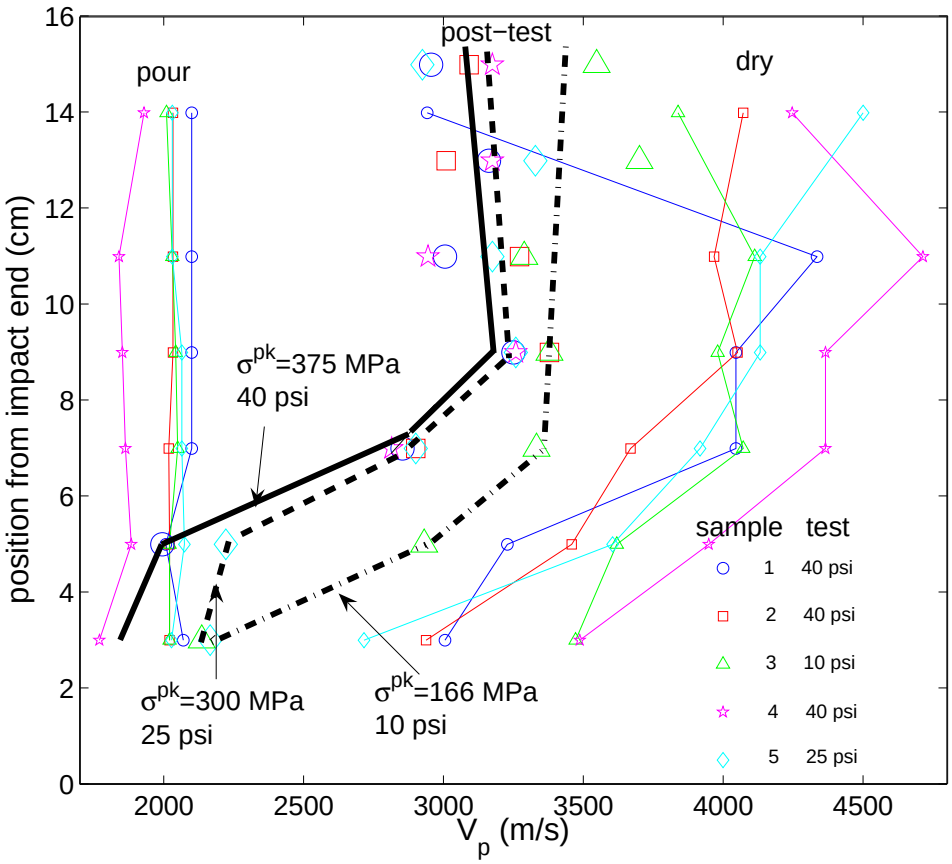

Figure 4.5. Post-test radial V_p measurements for sample set <0819>. Interpretive profiles illustrate the relationship between wave propagation velocity differences and incident bar peak stress state (166, 300, and 375 MPa, respectively). Large symbols correspond to post-test measurements. The *dry* pre-test V_p data are artificially high as discussed in the text.

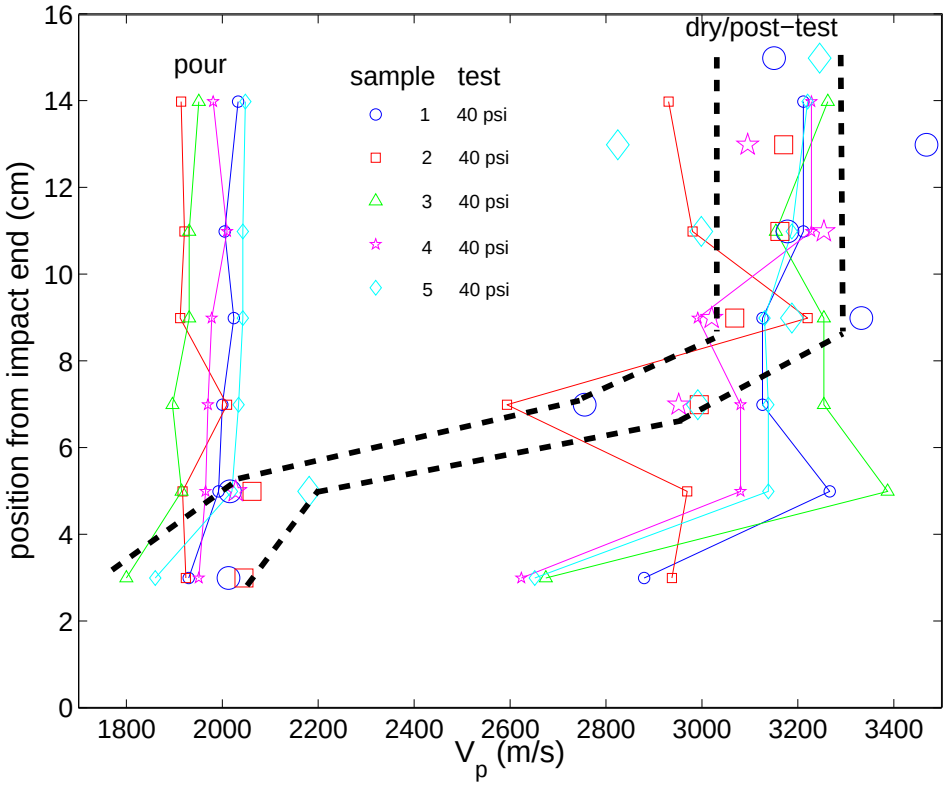

Figure 4.6. Post-test radial V_p measurements for sample set <0811>. Interpretive profiles define the bounds of wave propagation velocity differences observed with incident bar peak stress of 375 MPa. Large symbols correspond to post-test measurements.

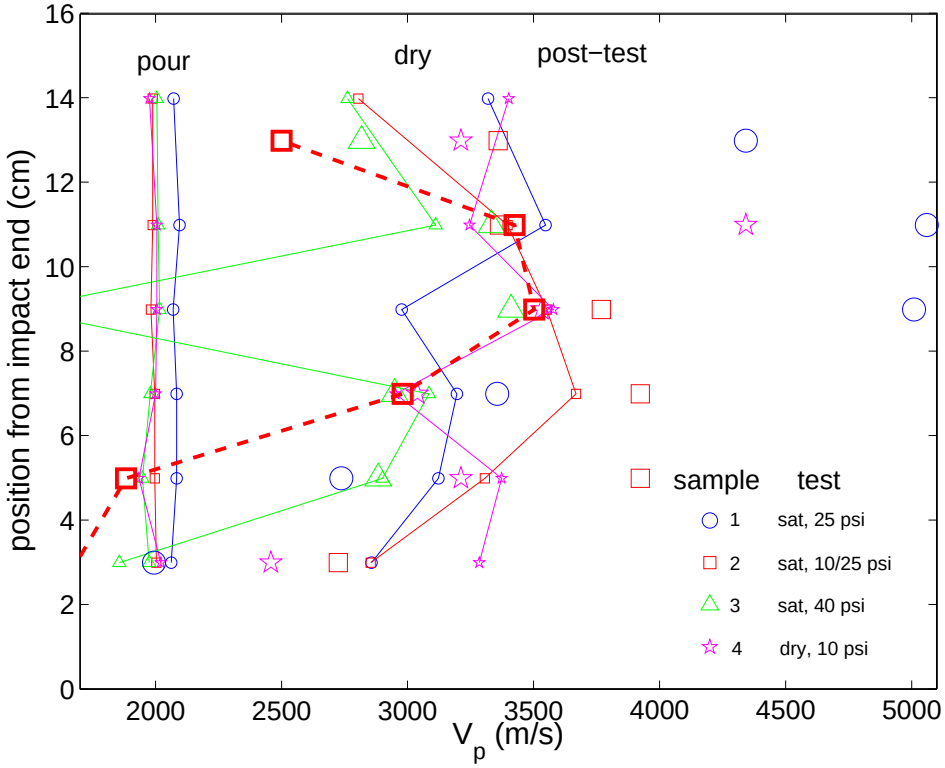

Figure 4.7. Post-test radial V_p measurements for sample set <0906>. These results illustrate the complex influence of saturation and P_{br} on wave propagation velocities. Samples 1 and 2 show significant high-frequency fluid effects. Sample 2 tested at P_{br}=25 psi is shown by bold squares connected by heavy dashed line. Large symbols correspond to post-test measurements.

Chapter 5

Discussion

Two topics will briefly be addressed relative to the results shown in Chapter 4. First, a simplified analysis of the energy propagation in a typical dry sample is developed to help identify the extent and effective velocity of the plasticized wavefront, and to explain the observed energy dispersion. Second, a comparison is made between the post-test V_p measurements (Table 4.1) and results from large-scale explosively-loaded concrete tests (Holcomb et al., 2005).

5.1 Energy propagation and plastic work

Rigorous interpretation of the momentum trap strain waveforms (Figures 4.1- 4.3) is extremely complicated and would require a sophisticated inverse modeling approach in which the constitutive dynamics of the interfaces and sample material could be explicitly represented. To first order, however, such issues can be side-stepped by assuming (i) the effective interfaces described for analysis of the hammer tests *disappear* by the time the incident bar has reached its peak particle velocity at the bar-sample contact, and (ii) that the wave propagation velocity structure can be modeled as time-independent. The first assumption is reasonable given the fact that the incident bar end would translate 50-200 μm within the $\sim$14 μs rise time for the range of incident stress wave conditions tested. The second assumption follows from the definition of an elastic-plastic transition state in the concrete. Figure 5.1 shows the forward model results for an incident bar-sample-momentum trap as parameterized for analysis in Chapter 2, except for the substitution of a concrete sample (18 cm long) with a variable-length plastic zone extending from the incident bar to 1-2 cm into the sample. Although the modeled incident waveform is longer in duration than that used for the actual experiments, the resulting waveforms clearly reproduce the dispersive nature and key characteristics of the test waveforms. As shown in Figure 5.1, the dispersion of the incident wave is due to energy trapped in the adjoining plastic zone by the higher impedance materials of the incident bar and non-plasticized sample material (von

Karman and Duwez, 1950; Kolsky, 1963). In reality, the transition is likely gradational, with its spatial sharpness defined approximately by the local, or strain-dependent, slope of the unconfined–or low-stress confined–uniaxial compression curve which defines the effective strain-dependent Young's modulus. Model results based on a plastic wave propagation velocity of 500 m/s, with a plasticized zone of 1.5-2.0 cm, appear to reasonably match the stress-time curve shape for experimental results associated with σ_{inc}^{pk} ~375 MPa. Note that this wave velocity, combined with an assumption that approximately half of the original porosity within the plastic zone is consumed when the concrete is plasticized, suggests an effective Young's modulus of 0.5-0.6 GPa. This is only ~2.5% of the original elastic value.

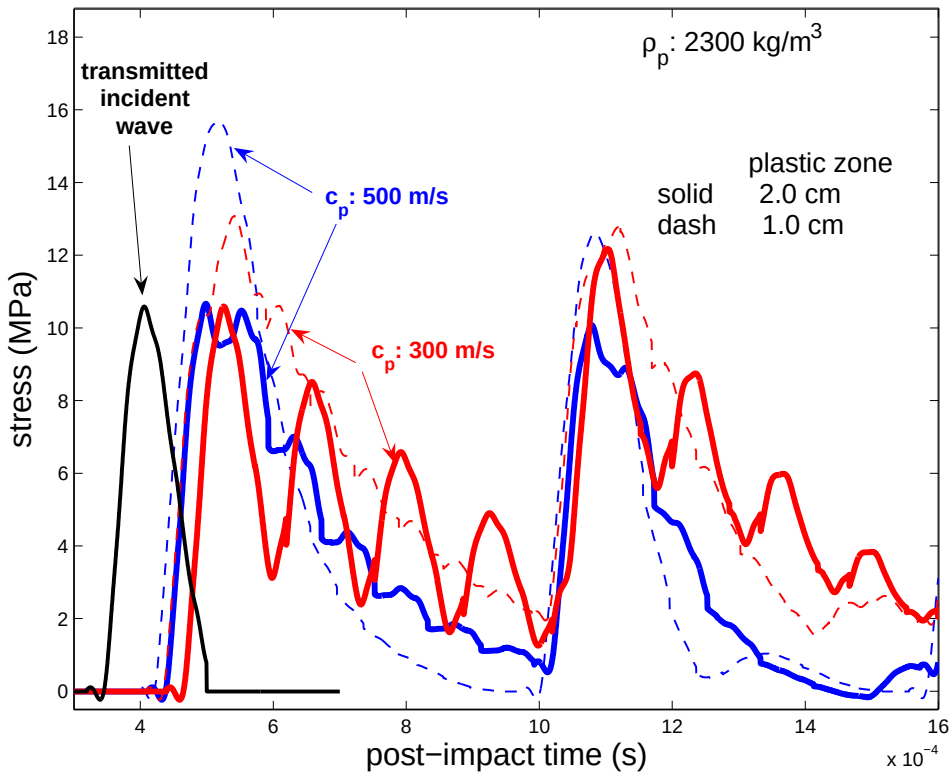

Figure 5.1. Apparent energy dispersion observed in momentum trap strain can be explained by formation of a plasticized zone (1-2 cm length) developed by the translation of the incident bar into the concrete sample.

This plastic zone length is consistent with the plasticized pore volume results (V_{cr}) obtained from Table 4.1, which when converted to an effective depth suggest that penetration extends 1.5-2.0 cm into the sample front (Figure 5.2). Figure 5.2 also highlights the effects of fluid saturation, with higher saturation states appearing to suppress the plasticity formation below incident particle velocities of ~13.0 m/s.

5.2 Comparison to previous penetrator-simulation field tests (SAND2004-5211)

Changes in pre- and post-test V_p measurements (Figures 4.5- 4.7; Table 4.1) offer the most direct comparison to establish a similarity in analog laboratory-field testing (Table 7 and Figure 66, respectively; Holcomb et al., 2005). The extent of the region of severe microstructural change as evidenced by the elastic wave velocity perturbations ranges from 0, for v_{part} <13.0 m/s under saturated conditions, to ∼8 cm, for v_{part} <16.7 m/s under dry conditions. Elastic wave-based Young's moduli are reduced to as low as 8 GPa for the ∼1 cm-long interval immediately adjacent to the plasticized region, for the samples tested here. The results for the multi-aged concrete cores recovered from the explosive tests reported in Holcomb et al. (2005) show a highly damaged zone extending 5-10 cm in from the borehole wall. The degree of V_p perturbation is quite variable from cylinder to cylinder. At least qualitatively, however, the stress states subjected to the near-wall materials in the explosively-loaded concrete cylinders, and those produced in the modified SHPB/impact-test samples, appear to be similar.

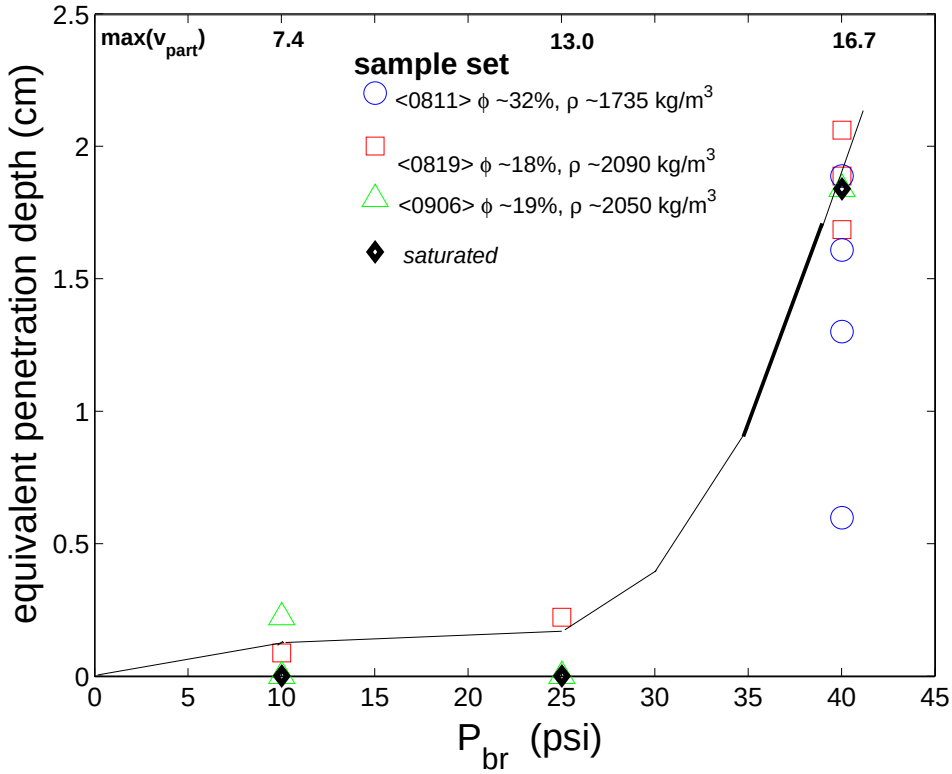

Figure 5.2. Effective *penetration* depth as a function of P_{br}, or its equivalent peak penetrator particle velocity (v_{part}; m/s). Penetration depth was estimated by dividing the estimated total pulverized concrete volume by the area of the incident bar face. This result is consistent with the concept of a critical velocity in plastic deformation propagation (von Karman and Duwez, 1950) and the abrupt deceleration transition data as shown and modeled in Forrestal (1986). A qualitative fit to the penetration depth-particle velocity data for the 19% porosity samples is sketched for illustrative purposes only.

Chapter 6

Conclusions and recommendations

A modified SHPB/impact test apparatus has been successfully prototyped for generating reproducible plastic-anelastic-elastic energy propagation states within a weak concrete, consistent with conventional cavity expansion modeling and analysis. Analysis of pre- and post-test microstructural integrity, through V_p measurements, and simplistic 1D modeling of dynamic stress-time waveforms clearly delineate the spatial extent of these propagation states. For the range of incident peak stress (160-370 MPa), or equivalent incident bar strain rates of 100-240 $s-1$, the disturbed region extends 4-8 cm into a sample with the zone of plastic deformation including the first 0-2^+ cm of that interval. The results suggest a critical particle velocity of 13.0-14.0 m/s is necessary to induce significant plastic deformation, though lower values (>7.4 m/s) still produce a damage zone that acts to disperse the incident stress wave to a clearly detectable extent. An unfortunate aspect of the experimental design is the effective discontinuity that occurs at the incident bar-sample and sample-momentum trap interfaces. This artifact complicates analysis and interpretation of the dynamic stress-time waveforms by adding a time (or strain) dependency in the transport of energy across these boundaries. These complications will probably not be completely overcome for complex porous media such as concretes, though easily-machined engineering materials should not suffer greatly as the average interface aperture can be made smaller than the translation distance of the incident bar end during the initial pulse rise time.

The following recommendations would significantly increase the information that could be obtained from these analog experiments:

- Develop a 1D numerical forward model that accounts for the dynamic constitutive behavior, including poroelastic effects, of the tested materials. The complete incident bar-sample-momentum trap would be discretized at possibly variable resolution so that sharp changes in material type (e.g., at the incident bar-sample interface) could be properly treated.

- Develop *in situ* pressure response calibration, particularly for the stress-rise portion of the incident wave, for each pinducer imbedded in a sample.

With an accurate *independent* stress-time measurement from within the sample, and a forward model capable of representing a wide range of static to dynamic constitutive behaviors (e.g., the Geomodel [Fossum, 2004]), a nonlinear inverse problem formulation could be solved to find an optimal space-time constitutive and physical property parameter set that explains the strain-/stress-time observations made on the incident bar, in the sample, and on the momentum bar. This advancement would be a definitive improvement over the simpler, even arbitrary, material representations used currently in cavity expansion models that dominate the penetrator literature today.

References

[1] Forrestal, M.J. Penetration into dry porous rock. *Int. J. Solids Structures*, 22(12):1485–1500, 1986.

[2] Forrestal, M.J., D.J. Frew, J.P. Hickerson, and T.A. Rohwer. Penetration of concrete targets with deceleration-time measurements. *Int. J. Impact Engin.*, 28:479–497, 2003.

[3] Forrestal, M.J. and D.Y. Tzou. A spherical cavity-expansion penetration model for concrete targets. *Int. J. Solids Structures*, 34(31-32):4127–4146, 1997.

[4] Fossum, A.F. Rock penetration: Finite element sensitivity and probalistic modeling analysis. Technical report SAND2004-3926, Sandia National Laboratories, Albuquerque, New Mexico 87185 and Livermore, California 94550, August 2004.

[5] Frew, D.J., M.J. Forrestal, and J.D. Cargile. The effect of concrete diameter on projectile deceleration and penetration depth. Technical report SAND2004-xyza, Sandia National Laboratories, Albuquerque, New Mexico 87185 and Livermore, California 94550, unknown 2004.

[6] Frew, D.J., M.J. Forrestal, and W. Chen. Pulse shaping techniques for testing elastic-plastic materials with a split hopkinson pressure bar. *Exp. Mechanics*, 45(2):186–195, 2005.

[7] Gran, J.K. and D.J. Frew. In-target radial stress measurements from penetration experiments into concrete by ogive-nose steel projectiles. *Int. J. Impact Engin.*, 19(8):715–726, 1997.

[8] Holcomb, D.J., A.F. Fossum, G.L. Gettemy, R.D. Hardy, D.R. Bronowski, R.R. Rivas, and D.S. Preece. Geomechanics of penetration: Experimental and computational approaches- Final report for LDRD Project 38718. Technical report SAND2004-5211, Sandia National Laboratories, Albuquerque, New Mexico 87185 and Livermore, California 94550, January 2005.

[9] Kolsky, H. *Stress Waves in Solids*. Dover, New York, 1963.

[10] Krautkramer, J. and Krautkramer, H. *Ultrasonic Testing of Materials (3rd edition)*. Springer-Verlag, New York, 1983.

[11] Olsson, W.A. and D.J. Holcomb. Compaction localization in porous rock. *Geophys. Res. Lett.*, 27(21):3537–3540, 2000.

[12] Pyrak-Nolte, L.J., L.R. Myer, and N.G.W. Cook. Transmission of seismic waves across single natural fractures. *J. Geophys. Res.*, 95(B6):8617–8638, 1990.

[13] Silk, M.G. *Ultrasonic transducers for nondestructive testing*. Adam Hilger Ltd., Bristol, 1984.

[14] von Karman, T. and P. Duwez. The propagation of plastic deformation in solids. *J. App. Physics*, 21:987–994, 1950.

[15] Warren, T.L., A.F. Fossum, and D.J. Frew. Penetration into low-strength (23 MPa) concrete: Target characterization and simulations. *Int. J. Impact Engin.*, 30:477–503, 2004.

[16] Zheng, S., U. Haussler-Combe, and J. Eibl. New approach to strain rate sensitivity of concrete in compression. *J. Eng. Mechanics*, 125(12):1403–1410, 1999.

DISTRIBUTION:

1 MS 0751
Larry S. Costin, 6111

1 MS 0751
Tom W. Pfeifle, 6117

3 MS 0751
David J. Holcomb, 6117

5 MS 0751
Glen L. Gettemy, 6117

1 MS 0372
Joseph Jung, 1527

1 MS 0893
John Pott, 1523

1 MS 0885
Justine E. Johannes, 1810

3 MS 9018
Central Technical Files, 8945-1

2 MS 0899
Technical Library, 9616

1 MS 0612
Review & Approval Desk, 9612

1 MS 0123
D. Chavez, LDRD Office, 1011